CIRP Annals - Manufacturing Technology 68 (2019) 575–578

Contents lists available at ScienceDirect

CIRP Annals - Manufacturing Technology

journal homepage: http://ees.elsevier.com/cirp/default.asp

A novel realization of diffractive optically variable devices using ultrasonic modulation cutting

Ping Guo [a,*], Yang Yang [b]

[a] Department of Mechanical Engineering, Northwestern University, Evanston, IL, USA
[b] Department of Mechanical and Automation Engineering, The Chinese University of Hong Kong, Hong Kong

Submitted by Serope Kalpakjian (1), Boise, USA

ARTICLE INFO

Keywords:
Micro machining
Vibration
Optically variable device

ABSTRACT

Optically variable devices (OVDs) enable the angle-dependent optical effect for anti-counterfeiting. This paper proposes a multi-image encoding strategy and demonstrates single-, two-, and three-layer OVDs using ultrasonic modulation cutting. An analytical model that incorporates the diffractive intensity spectrum, resonance characteristics of diffraction efficiency, and grating geometry is presented to accurately predict the apparent color information in hue, saturation and brightness. Ultrasonic modulation cutting is proposed for ultrafast pixel-level rendering by tuning the grating spacing. Two-layer image encoding is achieved by interlacing gratings with spatially separated diffractive spectra, while a layer of relief image is added for three-layer image encoding.

1. Introduction

Optically variable devices (OVDs) have proven to be an effective solution for counteracting the fast-evolving counterfeiting activities [1]. The essential security feature of OVDs, as the name indicates, is the variability of their appearance with the changing viewing angle and/or illuminating condition, which makes them impossible to replicate by commercial photocopiers or digital scanners. The angle dependent appearance takes the form of color variation or sometimes switching between two totally different images. One of the underlying mechanisms accounting for the optically variable effect is the existence of surface structures and their complex diffractive interaction with illumination light [2]. Carefully designed surface structures act as micro-gratings and diffract light with different wavelengths into different directions, thus enabling the iridescent color effect.

The long-standing challenges of realizing diffractive OVDs lie in the precision and efficient fabrication of surface micro-structures. Many researchers have been exploring new manufacturing processes towards achieving high-performance OVDs. Electron-beam lithography (EBL) has been utilized for structural color rendering by fabricating highly-ordered aluminum nanorods with controllable geometry [3]. Nevertheless, the lithography-based techniques are not only expensive and complex, but also limited in terms of sample size. Femtosecond laser-induced periodic surface structures (LIPSSs) are widely reported as an effective method for structural coloration of metals [4]. Selective display of angle-dependent patterns has been demonstrated utilizing the correlation between the LIPSS orientation and laser polarization direction [5]. The fundamental mechanism governing the LIPSS formation and distribution, however, is still not uncovered, preventing the prediction and optimization of overall optically variable effect. In addition, each layer of LIPSS patterns contains only a single-color component, which limits its encoding capability and security level for anti-counterfeiting.

In this paper, we, for the first time, demonstrate an efficient realization of OVDs for single-, two-, and three-layer image encoding using ultrasonic modulation cutting. A machined sample of two-layer image encoding is demonstrated in Fig. 1, where two complex images from Pokémon characters (Totodile and Squirtle) can be selectively displayed under different viewing angles. The brass workpiece (16×16 mm and 0.16 million pixels) was machined in 7 min.

We first present an analytical model that incorporates the diffractive intensity spectrum, resonance characteristic of diffraction efficiency, and grating geometry to predict the angle-dependent color hue, saturation and brightness information. Based on the analytical model, an encoding strategy is proposed

Fig. 1. Photos of the changing appearance of machined workpiece by slowly rotating the sample under the office light illumination condition.

* Corresponding author.
E-mail address: ping.guo@northwestern.edu (P. Guo).

https://doi.org/10.1016/j.cirp.2019.04.014
0007-8506/

by interlacing the gratings with spatially separated diffractive spectra, so that each image is selectively visualized in its designated viewing space. Ultrasonic modulation cutting is adopted to enable ultrafast pixel-level rendering of sub-micron gratings with controllable spacing. In the end, we further demonstrate a three-layer OVD by using the additional layer of relief image.

2. Modeling

2.1. Intensity distribution of blazed diffraction gratings

The ideal profile of a reflective type blazed grating can be described by its blazed angle (θ_b), effective working facet length (a) and spacing distance (d), as illustrated in Fig. 2(a). Assuming that light of wavelength λ is incident on the grating at an angle θ_i and diffracted at an angle θ_k, the intensity distribution of diffraction can be approximated based on the scalar theory [6] as:

$$\frac{I_{\theta_k}}{I_0} = \frac{\sin^2 u}{u^2} \cdot \frac{\sin^2 Nv}{\sin^2 v} \tag{1}$$

where I_o is the specular reflection intensity associated with the intensity of incident light and the material property of substrate; N is the number of grating grooves used for calculation. The equation describes the combined effect of diffraction of a single grating and of the interference of diffracted waves emanating from each grating, where u is half of the maximal optical path difference for the diffraction of a single grating and v is half of the phase retardance introduced by each grating. Their definitions can be derived according to the geometric relationship by Ref. [7]:

$$u = \frac{\pi a}{\lambda}[\sin(\theta_i - \theta_b) - \sin(\theta_k + \theta_b)] \tag{2}$$

$$v = \frac{\pi d}{\lambda}(sin\theta_i - sin\theta_k) \tag{3}$$

The resonant wavelength in the intensity spectrum can be derived by taking the first derivate of Eq. (1) with respect to the wavelength of the illumination light, which is reduced to the well-known grating equation (assuming $\theta_k = 0$):

$$dsin\theta_m = K\lambda_r \tag{4}$$

where λ_r is the resonant wavelength; K is an integer indicating the diffraction order. The grating equation alone is not sufficient to describe the apparent color, since it is essentially a one-dimensional projection of the three-dimensional color space.

Following Eqs. (1)–(3), an intensity distribution map of gratings with spacing distances of 0.45 μm, 0.75 μm, and 1.05 μm is illustrated in Fig. 2(b) in the classical-diffraction mount ($\varphi = 90°$) and at the normal viewing angle ($\theta_k = 0$). Different combinations of grating spacing, incident angle and diffraction order can be selected for rendering the desired structural color with a given resonant wavelength. From the figure, we notice the following points: (1) The overall intensity is significantly reduced with the second order diffraction compared with the first order as illustrated by the case of 1.05 μm curves in Fig. 2(b). The maximal

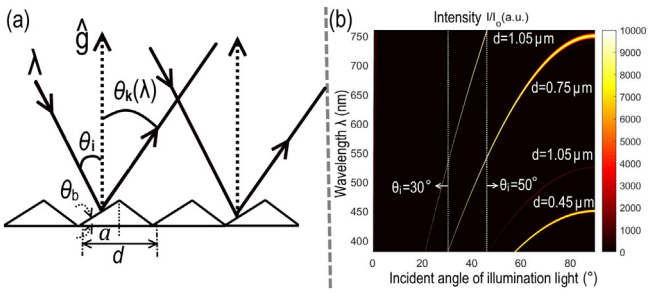

Fig. 2. (a) Geometric definition of the reflective-type diffraction grating; and (b) intensity of the first order diffraction for a different grating spacing shows no remarkable difference; (2) The incident angle range of illumination light that brings diffraction resonance shows a strong dependence on the grating spacing. The incident angle range for the first order resonance reaches its maximum range from 30° to 90° when the grating spacing is at 0.75 μm (the upper limit of the visible spectrum), while the location of incident angle range moves towards the right with the decrease in grating spacing. In addition, when the grating spacing is smaller than 0.75 μm, the first order resonance curve cannot cover the whole visible spectrum but only reaches the wavelength up to the grating spacing. For the case of 0.45 μm curve, the incident angle range is from 58° to 90° for the resonance of light from 380 nm (the lower limit of the visible spectrum) to 450 nm; and (3) The resonance quality factor can be intuitively described by the line width of the resonance curves in the figure, where a narrower line width corresponds to a higher resonance quality factor (1.05 μm). It mostly affects color saturation.

2.2. Encoding strategy

The derived correlation between the grating spacing and the overall structural color effect in Section 2.1 provides guidance for rendering complex images and encoding multi-image information.

When single-layer image encoding is desired based on the iridescent effect, a specific viewing angle can be assigned to design the grating distribution using the diffractive intensity spectrum. For example, when looking at the vertical line fixed at an incident angle of 50° in Fig. 2(b), we can determine the resonant wavelength for a specific grating spacing by looking at the intersection coordinate between the vertical line and the resonance curve. In addition, due to the finite incident angle range, only gratings with a spacing distance between 0.50 μm and 1.0 μm can introduce the first order resonance or appear as a certain color at this particular incident angle. We then can construct a grating spacing matrix corresponding to the prescribed color at each pixel. The original image will be replicated with a high similarity at the designed illumination angle, while exhibiting synchronous color shifting with the change of illumination angle. This color variation is also predictable based on the derived optical model.

Built on the idea of finite incident angle range, a strategy for two-layer image encoding is to design the grating distribution for two images with spatially separated spectra, or say, non-overlapping incident angle ranges. For example, if we specify two particular illumination angles at 30° and 50° as shown in Fig. 2(b), the 1.05 μm grating will only resonate at 530 nm in the visible spectrum for the illumination angle of 30°, while the 0.75 μm grating will only resonate at 575 nm for the illumination angle of 50°. We identify the grating spacing ranges from 0.50 μm to 1.0 μm whose resonance curve intercepts the vertical line at $\theta_i = 50°$ and from 0.76 μm to 1.52 μm for the incident angle of 30°.

In the demonstrated example of two images consisting of Squirtle and Totodile, we have assigned gratings with the spacing of 0.3 μm, 0.65 μm, 0.75 μm and 0.88 μm to Squirtle, and gratings with the spacing of 0.3 μm, 1.05 μm, 1.15 μm and 1.25 μm to Totodile. The 0.3 μm grating is selected as the background color since its diffraction intensity under the designed viewing conditions can be ignored. Then, all the odd lines of the Squirtle matrix and all the even lines of the Totodile matrix are alternatively interlaced line-by-line to obtain the overall mixed grating distribution. Although the two groups of gratings representing the two-layer images are interlaced in the same region, only one of them can be individually displayed under different illumination angles due to the spatially separated diffractive spectra. As the typical angular resolution of the naked human eye is an arc minute, so the best discernible distance can reach around 80 μm at a normal observing distance. An isotropic pixel size of 40 × 40 μm is adopted during the encoding process for process demonstration. The overall encoding strategy for two-layer OVDs can be summarized by Fig. 3.

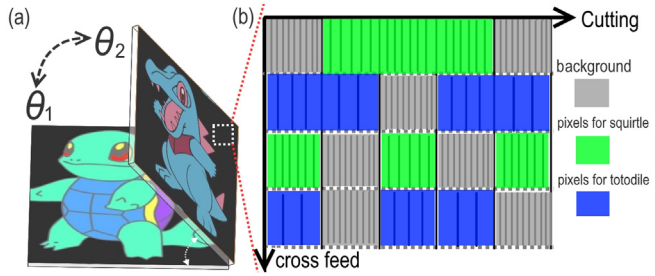

Fig. 3. Encoding strategy for two-layer OVDs: (a) optically variable effect of

2.3. Simulation of optically variable effect

We build a rendering simulation model to accurately predict the apparent color of grating-induced structural coloration and performance of OVDs by incorporating the three-dimensional color information in HSV (hue, saturation, value/brightness) representation. We choose the HSV representation due to the independence of each axis in HSV coordinates [6]. In addition, by considering the resonance nature of grating-induced structural coloration, we can directly relate the hue, saturation, and brightness to the characteristic parameters in the diffractive intensity spectrum as shown in Fig. 2(b).

The color hue is usually regarded as a digital analog of the dominant wavelength of spectral color, which is related to the resonant wavelength in the intensity spectrum as described by Eq. (4). The resonant wavelength is then mapped to the hue axis with a calibrated transfer function [8].

The color saturation is determined by a combination of the light intensity and how much it is distributed across the spectrum of different wavelengths [8]. Highly saturated color is achieved by single-wavelength light at a high intensity. It is related to the quality factor of the resonance curve in the intensity spectrum, which is approximated by the ratio between the intensities at the resonance and waists as:

$$S = \frac{I(\lambda_r)}{I(\lambda_r - \Delta\lambda) + I(\lambda_r + \Delta\lambda)} \tag{5}$$

where λ_r is the resonant wavelength; and $\Delta\lambda$ is assumed to be 9 nm.

The color brightness is determined by the intensity at the resonant wavelength, which is given by inserting the resonant wavelength λ_r into Eq. (1).

When the grating distribution, viewing and illumination conditions are specified, the prediction of color appearance can be achieved by constructing the respective hue, saturation and brightness layers. The simulation results of the design example of Squirtle and Totodile are shown in Fig. 4. The grating distribution is

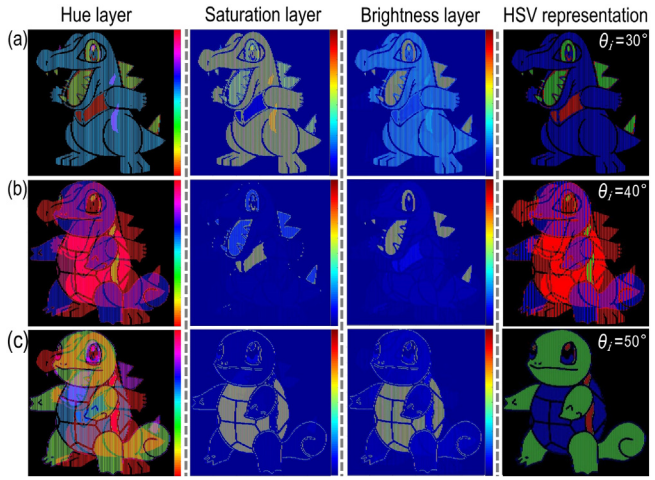

Fig. 4. Simulation of the angle-dependent appearance of the two-layer OVD (400 × 400 pixels) and its corresponding color components of hue, saturation and brightness under different incident angles of illumination: (a) $\theta_i = 30°$; (b) $\theta_i = 40°$; and (c) $\theta_i = 50°$.

assigned according to the encoding strategy described in Section 2.2. Additional parameter settings needed for the simulation include the number of grating grooves $N = pixel\ length/d$, and the blazed angle $\theta_b = 20°$ and effective working facet length $a = 0.5d$, which are determined from the actual machined grating profile. It is noted that the black background in the hue layer and overall appearance results from the 0.3 μm grating, which could not introduce any resonance in the visible spectrum. The hue layer alone may include both Squirtle and Totodile (mainly due to the higher order resonances) as seen in Fig. 4(c), but by combining the saturation and brightness layers, the predicted apparent view will only contain the portrait of Squirtle.

3. Experiments

3.1. Ultrasonic modulation cutting

Ultrasonic modulation cutting is introduced here for ultrafast pixel-level rendering of sub-micron gratings with controllable spacing. As illustrated in Fig. 5, the cutting tool follows an ultrasonic elliptical trajectory and is fed along an overlapping tool trajectory when it is coupled with a relatively slow nominal cutting velocity. The bottom half of the trajectories will be replicated on the machined surface forming a scallop-like surface. The resulting parallel grooves can act as diffraction gratings with tunable geometry [9]. By fixing the tool vibration frequency, the grating spacing d can be easily adjusted by modulating the nominal cutting velocity. The process parameters can be determined by commanding the cutting tool with the calculated nominal cutting velocity, while the cross feed (equals to the pixel width in cross-feed direction) and nominal depth of cut are kept unchanged during the single- and two-layer image encoding.

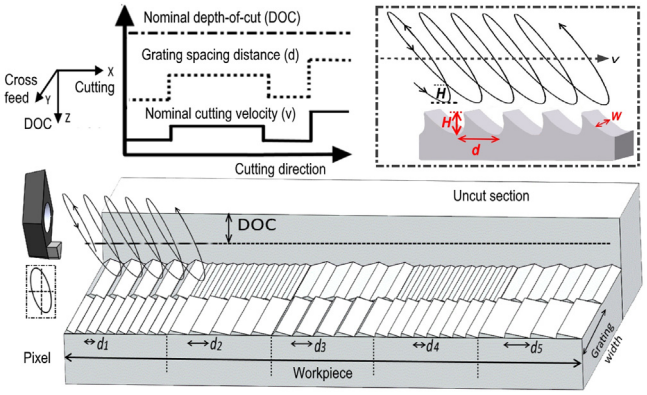

Fig. 5. Schematic of the ultrasonic modulation cutting process.

Compared with the traditional ruled gratings, the proposed technique addresses three long-standing challenges in micro-machining of diffraction gratings. Firstly, it enables easy adjustment of grating spacing at each pixel, which cannot be achieved by the ruling method. Secondly, it circumvents the minimum chip thickness effect. The grating height is independent of the nominal depth-of-cut, so by setting a large depth-of-cut, the effective uncut chip thickness is much larger than the feature size of the gratings. Lastly, the ultrasonic vibration frequency of the tool significantly increases the process efficiency, such that more than 30,000 lines of gratings will be generated per second. On the flip side, the machining accuracy and the grating profile control with the proposed technique still cannot compete with the conventional ruling method, but it brings the direct-writing capability necessary for fabricating OVDs.

3.2. Single-layer and two-layer image encoding

Following the strategies described in Section 2, Fig. 6 shows the comparison of two brass samples encoded with single-layer and two-layer images of the same machined area (16 × 16 mm) and the same resolution (400 × 400 pixels). Brass was selected to demonstrate the proposed technology due to its good machinability and

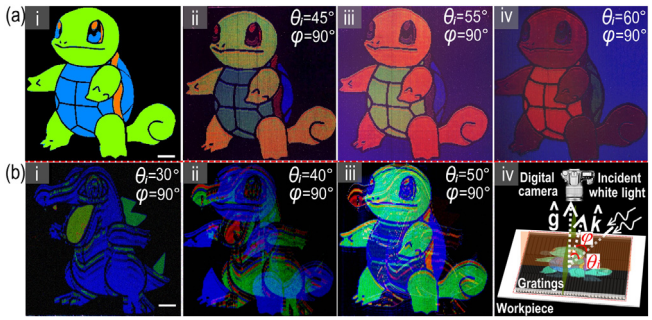

Fig. 6. Optically variable effect recorded at the normal viewing angle ($\theta_b = 0°$) but with different incident angles of illumination (azimuth angle fixed at $\varphi = 90°$): (a) single-layer OVD with (i) simulated image; (ii) $\theta_i = 45°$; (iii) $\theta_i = 55°$; (iv) $\theta_i = 60°$; and

high reflectivity. An isotropic pixel size of $40 \times 40\ \mu m$ is adopted for the process demonstration. The vibration tool works at 35.6 kHz with a vibration amplitude of 5 μm, so the nominal cutting velocity is modulated between 10.7 mm/s to 44.5 mm/s to achieve grating spacings from 0.3 μm to 1.25 μm. The nominal depth-of-cut is kept at 2 μm, while the cross-feed is 40 μm to match the pixel size. The vibration tool is incorporated into an XYZ positioning stage with a nominal resolution of 1 nm. Two single crystal diamond inserts are used for single-layer and two-layer encoding, which have a nose radius of 200 μm and 500 μm, respectively. All images are captured using a digital single-lens reflex (DSLR) camera at a normal angle ($\theta_k = 0$) in a dark room, as illustrated in Fig. 6(b)(iv). The azimuth angle is kept at 90° in the classical-diffraction mount, while the altitude angle (θ_i) of white light illumination is adjusted.

As shown in Fig. 6(a), the single-image OVD is achieved by the angle-dependent color variation. The color appearance of reproduced Squirtle shows a strong iridescent effect (ii-iv) and matches the designed image (i). In addition, Squirtle can only be identified in the incident angle range from 45° to 60°. The two-layer OVD can switch between the two totally different images as illustrated in Fig. 6(b)(i-iii). Totodile is displayed at 30° and Squirtle is displayed at 50°, while the two interlaced characters can be identified at 40° (Supplementary material Video S1). The captured images match the simulation results in Fig. 4 with differences mainly in the transition state. The differences mainly come from the mismatch between the assumed perfect blazed grating geometry and the actual imperfect grating profile.

3.3. Three-layer image encoding

We further demonstrate an extension of two-layer OVD to three-layer image encoding. The grating-induced structural colors are most evident in the classical-diffraction mount ($\varphi = 90°$) and vanished in the off-plane mount when the azimuth angle is 0°. In addition, the structural color effect is insensitive to the nominal depth-of-cut [9]. By combining these two unique features, we can engrave a third layer of information by adjusting the nominal depth-of-cut based on the gray value of an image at each pixel. The two-layer OVD can be displayed in the classical-diffraction mount, while the relief image can be seen in the off-plane mount. Fig. 7 demonstrates the machined sample with the two-layer OVD of Squirtle and Totodile and an additional grayscale image of a text logo of "AIM" and a swallow. The machining parameters were kept the same as for the two-layer OVD except for the depth-of-cut, which was modulated at three levels (2 μm, 4 μm, and 6 μm) according to the designed gray values of the engraved image. The added grayscale image will not influence the structural color effect when the diffraction is dominant as shown in Fig. 7(a)–(c), but it becomes apparent with no structural color when the illumination is parallel to the grating direction as shown in Fig. 7(d) (Supplementary material Video S2). It is worth mentioning that the image reproduction quality not only relies on the machining accuracy of sub-micron gratings, but also the encoding strategy and material optical property of OVD substrate. The long-term

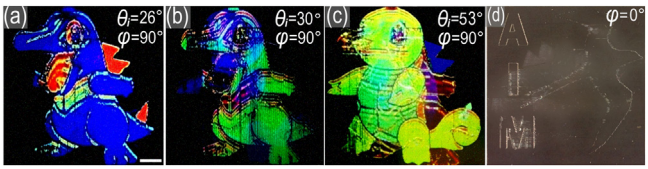

Fig. 7. Three-layer OVD recorded at the normal viewing angle ($\theta_b = 0°$) but with different incident angles of illumination: (a) $\theta_i = 26°$ and $\varphi = 90°$; (b) $\theta_i = 30°$ and $\varphi = 90°$; (c) $\theta_i = 53°$ and $\varphi = 90°$; (d) $\varphi = 0°$. Scale bar is 2 mm.

stability of generated OVDs can be improved by coating a transparent protective layer to prevent scratch and wear.

4. Conclusions

This paper presents a novel realization for diffractive optically variable devices. An analytical model has been developed to understand the essential characteristics of grating-induced structural coloration and to guide the overall grating distribution design for realizing multilayer OVDs. A simulation model has been derived to accurately predict the optically variable effect in HSV representation based on the intensity spectrum of diffraction gratings, resonance characteristics of diffraction efficiency, and grating geometry. Ultrasonic modulation cutting is adopted to enable ultrafast pixel-level rendering of sub-micron gratings with controllable spacing. Based on the proposed model, we have successfully demonstrated the manufacture of single-, two-, and three-layer OVDs. The single-layer OVD is simply achieved by the angle-dependent color variation. By interlacing two groups of gratings with spatially separated diffractive spectra, the two-layer OVD will switch between two different images when varying the illumination angle. Further, we show the three-layer OVD by adding an additional layer of relief image, which will be displayed in the off-plane mount.

Acknowledgements

This work was supported by the start-up fund from McCormick School of Engineering, Northwestern University, USA; and the Innovation and Technology Fund, Hong Kong, #ITS/076/17.

Appendix A. Supplementary data

Supplementary material related to this article can be found, in the online version, at doi:https://doi.org/10.1016/j.cirp.2019.04.014.

References

[1] Brinksmeier E, Gläbe R, Schönemann L (2012) Review on Diamond-machining Processes for the Generation of Functional Surface Structures. *CIRP Journal of Manufacturing Science and Technology* 5:1–7.
[2] Li J, Li G, Hu Y, Zhang C, Li X, Chu J, Huang W (2015) Selective Display of Multiple Patterns Encoded with Different Oriented Ripples Using Femtosecond Laser. *Optics and Laser Technology* 71:85–88.
[3] Olson J, Manjavacas A, Liu L, Chang W-S, Foerster B, King NS, Knight MW, Nordlander P, Halas NJ, Link S (2014) Vivid, Full-color Aluminum Plasmonic Pixels. *Proceedings of the National Academy of Sciences* 111:14348–14353.
[4] Malshe AP, Bapat S, Rajurkar KP, Haitjema H (2018) Bio-inspired Textures for Functional Applications. *CIRP Annals* 67:627–650.
[5] Li L, Hong M, Schmidt M, Zhong M, Malshe A, Huis B, Kovalenko V (2011) Laser nano-manufacturing–state of the art and challenges. *CIRP Annals* 60:735–755.
[6] Plataniotis KN, Venetsanopoulos AN (2013) *Color Image Processing and Applications*, Springer Science & Business Media.
[7] Casini R, Nelson PG (2014) On the Intensity Distribution Function of Blazed Reflective Diffraction Gratings. *JOSA A* 31:2179–2184.
[8] Yang Y, Guo P (2019) Global Tool Path Optimization of High-resolution Image Reproduction in Ultrasonic Modulation Cutting for Structural Coloration. *International Journal of Machine Tools and Manufacture* 138:14–26.
[9] Yang Y, Pan Y, Guo P (2017) Structural Coloration of Metallic Surfaces with Micro/nano-structures Induced by Elliptical Vibration Texturing. *Applied Surface Science* 402:400–409.